HYDRODYNAMICALLY UNSTABLE TURNING FLOW
IN THE END-SPACE OF A MAGNETICALLY GUIDED CNS CATHETER

Joseph A.C. Humphrey, Elisa Ferrante and George T. Gillies
Department of Mechanical
and Aerospace Engineering
University of Virginia
Charlottesville, VA 22904, USA
jach@virginia.edu, eaf4z@virginia.edu,
gtg@virginia.edu

Jorge L. Rosales
Phoenix Analysis and Design Technologies
ASU Research Park
7755 S. Research Dr., Suite 110
Tempe, AZ 85284
luis.rosales@padtinc.com

ABSTRACT

A study has been performed for the flow and heat transfer in the space between a pair of concentric tubes around the location where the fluid emerging from the inner tube turns 180° along the flat sealed end of the outer tube to proceed axially along the annular space between the tubes. Three Reynolds numbers and two end-flow spacings are investigated for the case with a solid ring externally mounted on the end of the inner tube. In the calculations the ring experiences uniform energy generation to simulate ohmic heating and its temperature field is a function of the flow-thermal field coupling. The results reveal a flow field that is 2D and steady at low Reynolds but which quickly becomes 3D and unsteady-chaotic at higher Reynolds. The findings are important for the development of fluid-cooled magnetically-guided catheters used for drug delivery as well as interventional procedures within the endovasculature and the neurovasculature. Because of page limitations, this paper focuses on the fluid mechanics results for an isothermal flow and a single end-flow spacing.

INTRODUCTION AND RELATED WORK

The overarching goal of this continuing investigation is to measure and calculate the thermofluids characteristics of the hydrodynamically unstable coolant flow in a magnetically-guided catheter used for drug delivery and interventional procedures within the endovasculature and, especially, within the neurovasculature (brain, spinal column). A better understanding of these characteristics should help improve the design of catheters for clinical applications. The goal is to develop a flexible catheter with three mutually orthogonal microcoils embedded in its tip which, when energized in appropriate ratios of coil current, will create a net dipole moment that will enable steering of the catheter with respect to a large background magnetic field; see Gillies and Corwin (2002) for a discussion of such techniques. This would make it possible to navigate the catheter within the large static magnetic field of a magnetic resonance imager, thus guiding the flexible catheter within the body of a patient, thus allowing essentially real-time imaging and stereotactic localization of the catheter during interventional procedures. The process is one of inverting the normal mechanism of magnetic stereotaxis (Howard et al., 1996) in that the

magnetic actuators would now be *inside* the body as opposed to *around* it.

A clinically useful catheter would have a maximum outer diameter of less than 3 mm, and consist of two concentric flexible tubes, the outer one being sealed at its end. During the catheter navigation process, the inner tube would deliver cooling water to the microcoils inside the tip of the catheter, with the return flow passing through the inter-tube annulus. Once in position, the microcoils would be de-energized thus eliminating the need for coolant. The inner tube would then be used to deliver a diagnostic or therapeutic agent to the target location through a semi-permeable membrane surface on the wall of the outer tube. Dissipations of 10 to 20 W are required to provide the magnitude of magnetic coupling needed for navigational purposes in most MR systems. Empirical studies based on joule heating due to the wire resistance of prototype coils have shown that cooling water flow rates must be on the order of 1 ml/s to prevent temperature maldistributions and possible burn-out of the microcoils. This is in contrast to drug delivery rates of 5 μl/min that are typically employed for delivering chemotherapeutic agents to the peritumoral region of CNS neoplasms (Broaddus et al. 2001).

While the geometry of the present catheter configuration is similar to that of the bayonet-type heat exchanger previousy investigated by, for example, Minhas at al. (1995) and Minhas and Lock (1996), it differs in a very fundamental way. This is because of the heated microcoils embedded in the tip of the catheter which significantly alter the flow and thermal fields around them. Also, previous work on bayonet-type heat exchangers has primarily focused on correlating the overall pressure drop coefficient and the Nusselt number with the Reynolds number for different tube radius ratios, with little attention paid to the structure and dynamics of the 2D to 3D unsteady flow transition taking place in the turning end-space between the tubes.

PRELIMINARY CONSIDERATIONS

A schematic of the flow configuration of interest is shown in Fig. 1, discussed further below. Based on the Reynolds number of the flow in the inner tube ($Re_{ti} = U_{ti} r_i /v$), visualization in the range $100 < Re_{ti} < 2000$ reveals a strongly directed jet emerging from the inner tube. The jet expands radially, with significant changes in momentum due to shearing of the flow along the end wall of the outer
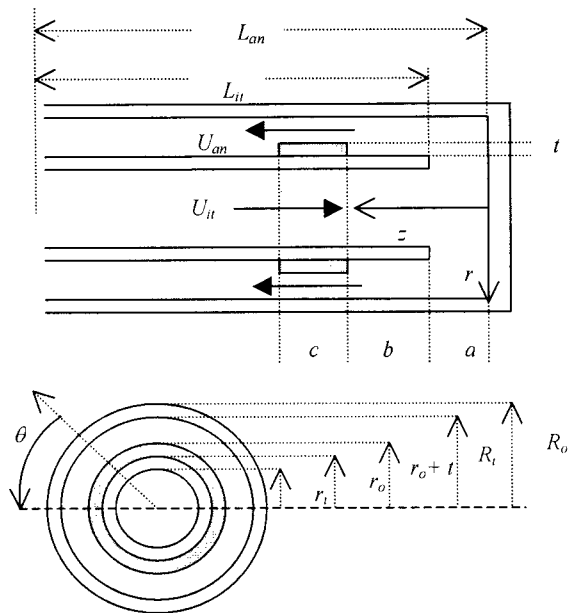
Fig. 1. Schematic of the concentric tube test section for the experiments (not to scale). Dimensions: $r_i = 5.1$ mm, $r_o = 7.5$ mm, $L_{it}/2r_i = 118$, $R_i = 41.3$ mm, $R_o = 44.2$ mm, $L_{an}/2(R_i - r_o) = 15.2$. The majority of cases investigated correspond to $a = 20$ or 40 mm; $b = 0$, $c = 10$ mm and $t = 8.1$ mm.

tube, and then rises along the inner wall of the outer tube. This turning motion induces a relatively large, doughnut-shaped recirculating flow region in the end-space, part of which is entrained by the jet and part of which passes over a ring on the inner tube in the inter-tube annulus. The details of the flows in these two regions, in particular the transition from a 2D steady state of motion to one that is 3D and unsteady, are strongly dependent on the values of Re_{it}, the geometrical parameter $r_i/(R_i + r_o)$ discussed below, and the dimensionless end-flow spacing, a/R_i.

Figures 2-a, and -b provide a feeling for the structure and dynamics of this motion. They are snapshots of the water flow in the test section, visualized by illuminating micron-sized guanine platelets (Kalliroscope Corp. AQ-1000 Rheoscopic Concentrate) with a thin, plane beam of white light. For the conditions of Fig. 2-a, the entire flow is laminar and steady, displaying a single, large, stable, axisymmetric (toroidal) vortex in the end-flow space. For the conditions of Fig. 2-b the motion in the end-flow space has become unsteady and 3D, and at higher Reynolds displays a wider spectrum of small-scale, highly vortical eddies in addition to three larger, temporally and spatially irregular toroidal vortices in the end-flow space.

It is easy to show from geometry that the Reynolds numbers of the flows in the inner tube ($Re_{it} = U_{it}\, r_i /\nu$) and the annulus ($Re_{an} = 2(R_i-r_o)U_{an}/\nu$) are related through the expression $Re_{an}/Re_{it} = r_i/(r_o+R_i)$. This ratio is always less than unity and it is equal to 0.105 for the present geometry. Thus, if the flow emerging from the inner tube is laminar, that downstream in the annulus will always be laminar. However, if the flow emerging from the inner tube is turbulent, depending on the value of $r_i/(r_o+R_i)$, that downstream in the annulus can be turbulent or laminar. Notwithstanding, as illustrated in Fig. 2-b, in this study we find the unusual condition that *the flow emerging from the inner tube can be laminar while that in the end-space can*
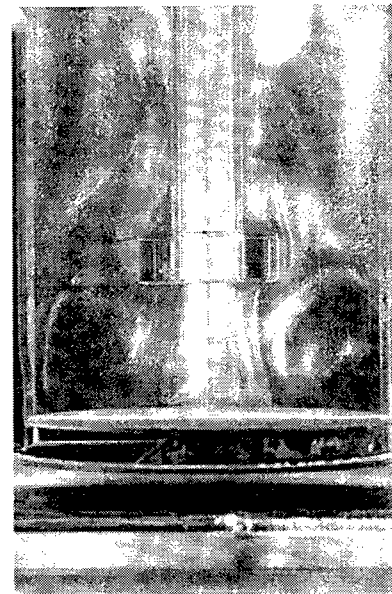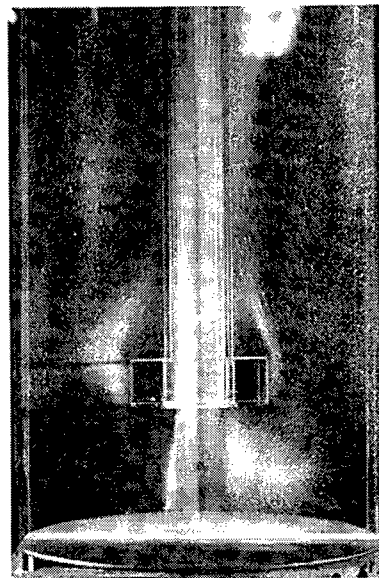

Fig. 2. Visualization of the end-flow region in the concentric tube test section for a case with a = 30 mm, b = 0, c = 10 mm, and t = 8.1 mm with: (top) $Re_{it} \approx 390$, $Re_{an} \approx 41$ (steady, 2D flow); and (bottom) $Re_{it} \approx 865$, $Re_{an} \approx 91$ (unsteady, 3D flow).

be highly unsteady, 3D and vortical (and, therefore, very "turbulent-like.") At least four conditions can contribute to this state: 1) at a sufficiently high Re_{it} the jet emerging from the inner tube and the radially-expanding flow it drives along the outer tube end wall are prone to shear layer instabilities; 2) at a sufficiently high (appropriately defined) Goertler number the main recirculating flow in the end-space is prone to centrifugal instabilities; 3) at sufficiently high Re_{an} the separated flow in the wake of the the ring surface facing the annulus exit plane becomes unstable; 4) at sufficiently high Re_{it} the recirculating flow in the end-space induces flow separation in the wake of the ring surface facing the outer tube end wall.

EXPERIMENTAL WORK

Apparatus and Test Section

The small dimensions required of a concentric tube catheter used for clinical applications make it very difficult to visualize or measure the flow and thermal fields in it, especially in the turning end-flow section containing the coiled wires used for magnetically induced stereotactic navigation. In order to perform flow visualization and particle image velocimeter (PIV) measurements, a geometrically scaled, transparent test section of the catheter corresponding to the dimensions given in Fig. 1 has been fabricated. The test section consists of an inner glass tube contained within an outer Plexiglas tube that is sealed at its end. The penetration depth of the inner tube into the outer tube is continuously variable. The inner tube is maintained in a concentric position with respect to the outer tube by means of a ring-shaped spacer with spokes. The spacer is placed in the annulus, towards the end of the inner tube but sufficiently downstream from the end-flow region so as not to affect it. The entire test section is aligned vertically and connected to a constant-head, recirculating water flow apparatus. The flow rate through the test section is determined with a calibrated flowmeter.

In addition to the flow visualization mentioned above, we have made field measurements of the instantaneous axial (v_z) and radial (v_r) velocity components from which the mean (V_z, V_r) and rms $(v_{z\ rms}, v_{r\ rms})$ values of these quantities, as well as the mean value of the circumferential component of vorticity (Ω_θ), have been obtained. All the PIV measurements have been made in an r-z plane passing through the symmetry axis of the test section. We have also performed numerical calculations of the 3D unsteady flow corresponding to the test section for isothermal and non-isothermal (heated ring) conditions. Here we report on a subset of the experimental and numerical results for isothermal flow conditions.

Measurement Procedure and Uncertainties

The working fluid is water at $20° \pm 1°$ C. The flow through the test section is controlled by a needle valve and measured with a rotameter to within $\pm$ 2%. The large length/diameter ratio of the inner tube guarantees fully developed flow conditions for the Reynolds number range investigated $100 < Re_{it} < 2000$. All linear distances in the test section are known to better than ± 0.5 mm.

A TSI Power View system is used to perform the PIV measurements. The system employs a pair of New Wave Solo Dual Nd:YAG lasers (50 mJ/pulse, 532 nm wavelength). An articulated arm with an optical head attached, consisting of a 200 mm spherical lens combined with a -15 mm cylindrical lens, is used to produce laser light sheets 46 mm high, and 0.04 mm at the waist with a divergence angle of 0.017 rad (1.75mm/100mm). The duration of a single laser pulse is 3-5 ns and the time between pulses ranges between 35 ms at low fluid velocities and 15 ms at high velocities. A Power View 4M Cross/Auto Correlation Digital CCD camera with an AF Nikkor 28 mm $f2.8$ lens set at an f-stop of 8 is used to capture the PIV images. The camera has 2K x 2K pixel resolution (12-bit digital output) at 17 frames/s. The system is controlled by a Laser Pulse Computer Controller Synchronizer interfaced to a Dual Processor Intel Xeon 2.0 GHz PC computer with 1 GB RAM and an 80 GB hard disk drive. TSI Insight 4 software is used for image acquisition and subsequent post-processing. Two-frame crosscorrelations are performed on 100 image pairs by means of FFT using a Gaussian peak search algorithm. The data are smoothed and outliers exceeding three standard deviations are removed. Flow statistics (mean and rms values of the axial and radial velocity components, and mean circumferential vorticity) are derived from the 100 image pairs obtained for each measurement case.

The sources and magnitudes of uncertainties affecting PIV measurements have been extensively documented in the literature; see, for example, Raffell et al. (1998) and the numerous references therein. We comment on those of relevance to this work. Hollow spherical glass particles, of diameter 8-12 microns and density $\rho_p \equiv 1.5$ g/cm^3, are used to seed the flow. Their theoretical (Stokes drag-based) relaxation time $(\tau_p = \rho_p d_p^2/18\mu)$ in water at 19 °C is $\tau_p < 1.2 \times 10^{-5}$ s. Since this time scale is several orders of magnitude smaller than the smallest time scale in the flow, particle lag is negligible. Uncertainties due to optical distortion caused by the curvature of the outer tube surface are minimized by immersing the turning end of the test section in a water-filled Plexiglas tank with flat walls. We estimate that this results in flow visualization and PIV images having less than 2% of optical distortion over 94% of their surfaces. The pulsed laser light sheets are carefully aligned to pass through the symmetry axis of the test section in the end-flow region, thus defining an r-z plane in which visualization and PIV images are obtained by aligning the optical axis of the camera normal to it. The goodness of this optical alignment is verified by comparing PIV measurements and calculations of the axial velocity component for fully developed, laminar (Poiseuille) flow conditions in the inner tube. Agreement between the two is better than 2% over the range $0 \le r/r_i \le 0.9$ but for larger values of r/r_i optical distortion affects the measurements in the inner tube. Uncertainties due to particle displacement in an interrogation subregion and the time between laser pulses are negligible. Variations in the field distributions of particle concentration from image to image are statistically averaged over the 100 image pairs. Because of the very large differences between the magnitudes of velocity in a) the jet emerging from the inner tube and b) the end-flow region between the inner and outer tube and around the ring in the annulus, the PIV imaging technique is optimized to accurately resolve *either* the flow in the jet *or* that in the end-flow region.

NUMERICAL WORK

Transport Equations, Boundary Conditions, Solution Procedure, Grid Refinement and Testing

The flow field is described by unsteady, 3D, constant property forms of the momentum and continuity equations. These are solved numerically subject to the following initial and boundary conditions: a) flow starting from rest, evolving to a "statistically stationary" state; b) impermeable, no-slip velocity boundary conditions along all solid surfaces; c) developed laminar flow at the inner tube inlet plane; d) developed (zero velocity gradient) flow at the annulus exit plane. An algebraic system of finite difference equations is obtained by volume integration of the conservation equations over staggered control volumes for the velocity components and pressure, respectively. The third-order QUICK scheme is used to approximate convection terms and second-order central differencing to approximate diffusion. A fully implicit, second-order, three-level scheme is used for time. Numerical solutions are obtained using the FAHTSO code (Rosales et al., 2000, 2001). This incorporates an adaptation of the

SIMPLE algorithm to obtain velocity and pressure. The modified strongly implicit procedure is used to solve the system of algebraic equations. The FAHTSO code has been tested extensively and the grid spacing and time steps employed in this investigation are set by reference to the extensive study of these effects for similar calculations of flows past square prisms in 2D channels with fixed walls, performed by Rosales et al. (2000, 2001). Present calculations are performed on a $110 \times 138 \times 36$ (r, z, θ) grid using a time step ranging between 0.005 and 0.010 s. The grid is non-uniform in the r and z coordinate directions and uniform in the θ direction. It is the most refined we can use to handle the volume of calculations performed in a reasonable amount of time. A typical run time on a DELL 620 computer with dual 933 MHz Pentium III processors takes about 80 hours for a converged solution corresponding to a physical time record 25 seconds long. We estimate that the accuracy of the computed flow fields lies within 5% of grid-independent results. Further details concerning the numerical procedure are provided in Rosales et al. (2000, 2001).

RESULTS AND DISCUSSION

Both the PIV experiments and the calculations presented here correspond to the configuration dimensions of Fig. 1 with $a = 20$ mm and $b = 0$ mm. The values of Reynolds explored are $Re_{it} = 250$, 500 and 1000. Because of the number of grid nodes required, the entry and exit lengths are set to $L_{it}/2r_i = 10.3$ and $L_{an}/2(R_i - r_o) = 1.8$ in the numerical calculations.

Calculated streamlines of the instantaneous flow (Fig. 3) show that it is steady-2D at $Re_{it} = 250$, mildly unsteady-3D and asymmetric at $Re_{it} = 500$, and markedly unsteady-3D and asymmetric at $Re_{it} = 1000$. In all cases, however, the jet emerging from the inner tube is highly directed and impinges on the center of the end wall of the outer tube. From here on the flow expands radially along the end wall to eventually curve upwards along the side wall of the outer tube to pass over the ring and exit the annulus. The streamlines, and corresponding plots of the vector velocity and circumferential component of vorticity (not shown), also reveal a large doughnut-shaped recirculating flow region in the end-space, and a much smaller one embedded in the corners of the outer tube. With increasing Re_{it} the flow separates, first at the downstream corner of the ring (facing the annulus exit plane), and then along its upstream surface, at a variable radial location between the inner tube radius and the outer radius of the ring. Also with increasing Re_{it}, the flow separates along the wall of the outer tube to create a third, very large but very weak, recirculating flow region.

Experimental results for the fields of mean vector velocity and mean circumferential component of vorticity, Ω_θ, are shown in Fig. 4. Very good agreement is observed with respect to corresponding calculations (not shown) of these instantaneous quantities in the flow. (Note that to obtain field distributions of mean quantities such as velocity and vorticity from the calculations would have been prohibitively costly in terms of computer storage and time.) Especially clear in the measurements are the two separated flow regions arising at the upstream and downstream corners of the ring and along the inner wall of the outer tube. The plots in Fig. 4 illustrate the extent of degradation in data image quality as the light sheets pass
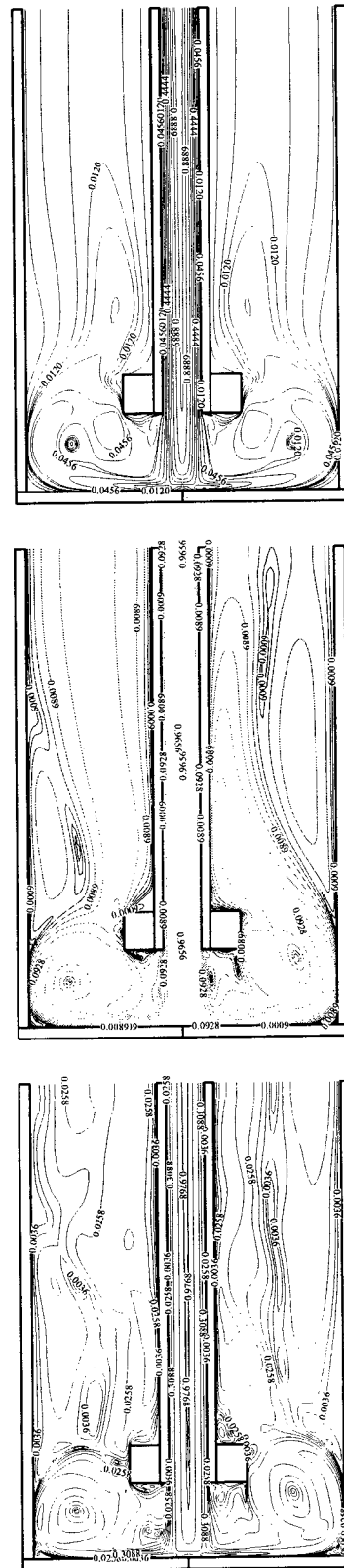

Fig. 3. Calculated streamlines in an r-z plane in the end-flow region of the concentric tube configuration for $Re_{it} = 250$ (top), 500 (middle), and 1000 (bottom).
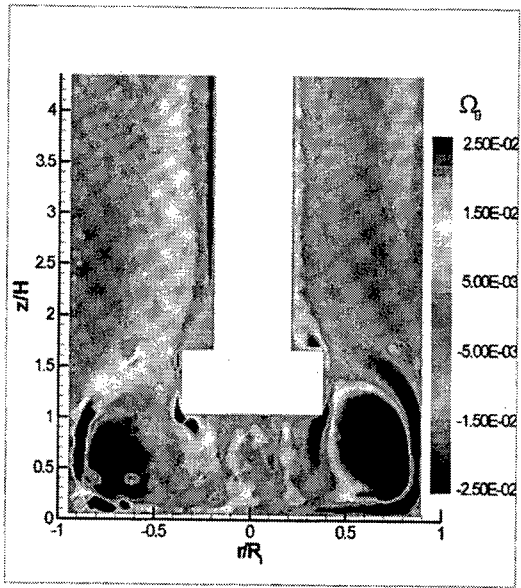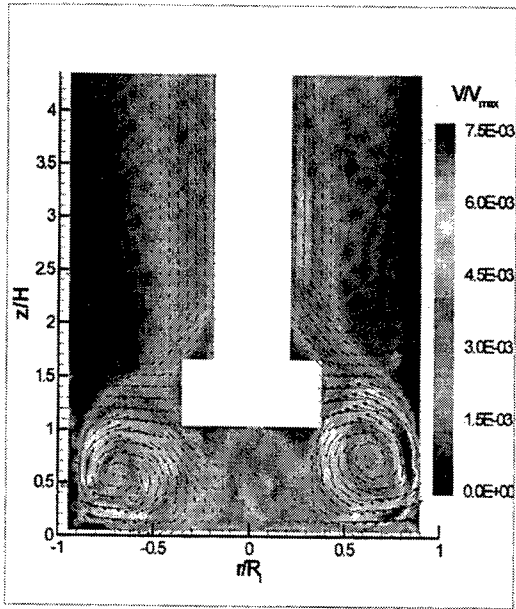
Fig. 4. Field values of the mean vector velocity with the magnitude of velocity superimposed (top), and of the mean circumferential component of vorticity (bottom), measured in an r-z plane in the end-flow region of the concentric tube configuration for Re_{it} = 500. The plots have been optimized to reveal the structure and intensity of the flow outside the jet (any details shown in the jet flow region should be ignored). Velocity is normalized by the maximum value in the inner tube, and vorticity by the value at the inner wall of the inner tube, for Poiseuille flow conditions. Note that H = a in the top figure (see Fig.1).

through an r-z measurement plane on the symmetry axis of the test section. In the figure, the pulsed laser sheets enter from the right, generally giving better definition of the flow on this side of the test section end-flow region.

Calculated time records of the three velocity components, at four circumferential locations 90° apart in the space between the ring and the outer tube wall, are shown in Fig. 5 for a flow with Re_{it} = 1000. The variations
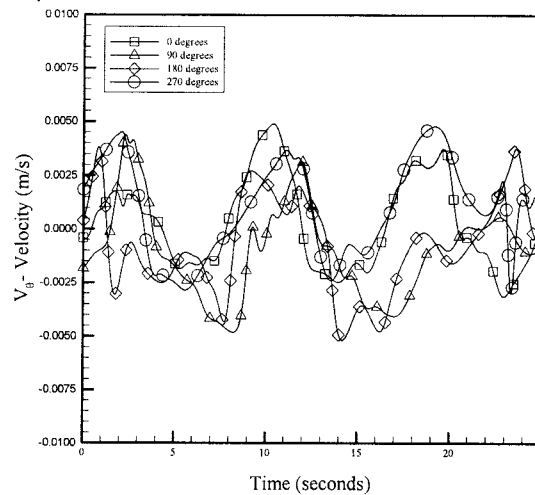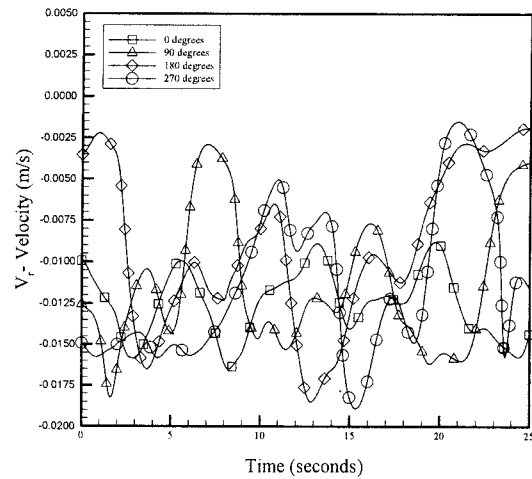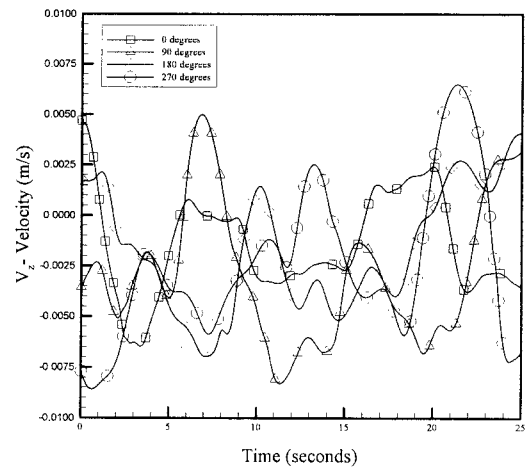

Fig. 5. Calculated time records of the instantaneous axial (top), radial (middle) and circumferential (bottom) velocity component at four points 90 degrees apart with coordinates $z = a + c/2$, $r = (r_o + R_i)/2$ and $\theta = 0°$, 90°, 180° and 270° in a flow with Re_{it} = 1000. See Fig. 1 to locate the coordinates of these points.

of velocity with time are pronounced. Those shown for the circumferential component suggest that, for the time record displayed, the flow oscillates back and forth, in phase, in the circumferential direction. However, at this value of Re_{it}, other time records of the circumferential velocity component and of the other two components are generally chaotic in appearance and do not show strong oscillation coherence among the four measurement locations. Irrespectively, typical flow oscillation time scales range in value between 2 and 10 s.

Statistics derived from the calculated time records are given in Table 1 in non-dimensional form. All four locations display essentially the same magnitude of velocity even though the sense of direction of the mean circumferential velocity component is positive at $\theta = 0°$ and 270°, and negative at 90° and 180°. At all locations, the radial component of velocity is the largest and is negative (directed inwards radially). The axial component is also negative (directed downwards axially). The signs of these components are in agreement with the sense of rotation of the recirculating flow in this region; see the coordinate system in Fig. 1 and the velocity and vorticity plots in Fig. 4. All three of the velocity components show large rms values relative to the local magnitude of velocity, the ones for the radial component again being the largest. Such large rms values are in agreement with the unsteady nature of this flow which displays relatively large length and time scales of a 3D, chaotic nature. Further analysis of this and related data is required, however, in order to determine the range of length scales in the flow and the energy distributed among these scales. Only then will it be possible to ascertain the degree to which this relatively low Reynolds number flow may be classified as "turbulent."

Variable Calculated (below)	θ Location (right)	0°	90°	180°	270°
$V_z\|_{max}$ (m/s)		0.17	0.17	0.17	0.17
$V_{mag}/V_z\|_{max}$		0.07	0.07	0.05	0.07
V_z/V_{mag}		- 0.12	- 0.25	- 0.19	- 0.21
V_r/V_{mag}		- 0.99	- 0.97	- 0.98	- 0.97
V_θ/V_{mag}		0.02	- 0.08	- 0.08	0.09
$\alpha = v_{z\,rms}/V_{mag}$		0.19	0.29	0.32	0.32
$\beta = v_{r\,rms}/V_{mag}$		0.16	0.34	0.52	0.39
$\gamma = v_{\theta\,rms}/V_{mag}$		0.17	0.18	0.24	0.19
$ke_f = \frac{1}{2}\,(\alpha^2 + \beta^2 + \gamma^2)$		0.05	0.12	0.21	0.15

Table 1. Numerically calculated statistics for the time records shown in Fig. 5. In the table, $V_z\|_{max}$ is the absolute value of the maximum velocity in the inner tube and V_{mag} is the absolute value (magnitude) of the velocity at the particular location in question.

CONCLUSIONS

While the present concentric tube geometry is well posed for experimental and numerical investigation, the flow in the turning end-space is surprisingly complex. At low Reynolds number ($Re_{it} = 250$) the flow is axisymmetric and steady, but for $Re_{it} > 500$ it becomes asymmetric, unsteady and 3D. In particular, while the flow at $Re_{it} = 1000$ appears chaotic, the degree to which it is "turbulent" remains unknown. As mentioned above, a number of instabilities may be associated with this

transition in state of motion. Of these, especially interesting is the possibility that at sufficiently high Re_{it} the recirculating flow in the end-space induces flow separation in the wake of the ring surface facing the outer tube end wall. The proximity of this separated flow to the shearing action of the jet emerging from the inner tube provides a mechanism for sustaining instabilities generated locally or convected into this region by the end-space recirculating flow.

This investigation demonstrates the usefulness of seeking guidance from experimentally validated computational simulations of the effect of geometry on the flow past the internal components of a catheter. Attention here has been limited to isothermal flow conditions but work is under way for the geometry of Fig. 1 for the case with a heated ring (Humphrey et al., 2003). The results from this type of study will help guide the design of the distal-tip micro-coils in magnetically steerable catheters, thus providing an important framework for improving the performance characteristics of such devices in the clinical setting.

REFERENCES

Gillies GT and Corwin FD 2002 "Microcoils in an MR imager: in situ study of electromagnetic effects in a triaxial coil catheter system," Technical Report No. UVA/640419/MAE03/101, SEAS, University of Virginia, Charlottesville, VA

Howard III MA, Grady MS, Ritter RC, Gillies GT and Dacey Jr. RG 1996 "Magnetic Stereotaxis: Image-Guided, Remote-Controlled Movement of Neurosurgical Implants," Clinical Neurosurgery 43: 382-391

Broaddus WC, Gillies GT and Kucharczyk J 2001 "Advances in Image-Guided Delivery of Drug and Cell Therapies into the Central Nervous System," Neuroimaging Clinics of North America 11: 727-735

Humphrey, JAC, Ferrante, E, Rosales, JL and Gillies GT "On the turning flow in the end-space of a concentric tube geometry with a heated obstruction," (in preparation)

Minhas H, Lock GSH and Wu M 1995 "Flow characteristics of an air-filled bayonet tube under laminar conditions," Int. J. Heat and Fluid Flow 16: 186-193

Minhas H and Lock GSH 1996 "Laminar-turbulent transition in a bayonet tube," Int. J. Heat and Fluid Flow 17: 102-107

Raffel M, Willert C and Kompenhans J 1998 "Particle Image Velocimetry – A Practical Gide," Springer

Rosales JL, Ortega A and Humphrey JAC 2000 "A numerical investigation of the convective heat transfer in unsteady laminar flow past a single and tandem pair of square cylinders in a channel," Num. Heat Transfer, Part A 38: 443-465

Rosales JL, Ortega A and Humphrey JAC 2001 "A numerical simulation of the convective heat transfer in confined channel flow past square cylinders: Comparison of inline and offset tandem pairs," Int. J. Heat and Mass Transfer 44: 587-603